Strain Measurement in the Spallation Target Using High-Radiation-Tolerant Fiber Sensors

Y. Liu, W. Blokland, C. Long, B. Riemer, M. Wendel, D. Winder

***Abstract*—We describe the measurement of fast dynamic strains in the mercury target module of the Spallation Neutron Source (SNS) using customized high-radiation-tolerant fiber-optic strain sensors. The sensors are made from fluorine-doped single-mode optical fibers that demonstrated high radiation tolerance at 1300 nm. A digital phase demodulation scheme is employed in the signal interrogation system, which enables high bandwidth measurement and has an excellent adaptability to sensor output power fluctuations and sensor gap variations. Fast transient strain waveforms induced by high-energy, high-intensity proton pulses are successfully measured. The sensors have survived radiation doses of 10^9 Gy. Both measurement bandwidth and radiation tolerance of the sensors are an order of magnitude higher than their commercial counterparts.**

***Index Terms*—Optical fiber sensors, sensor systems and applications, strain measurement, radiation effects, nuclear.**

I. Introduction

THE Spallation Neutron Source (SNS) target module is a stainless steel vessel through which mercury is pumped. Neutrons are produced through spallation reactions between the high-energy proton beam and the mercury. During a typical SNS operation, 1 ~ 1.4 MW (average power) proton beam is bunched to ~700 ns pulses at a 60 Hz repetition rate. The peak power of the proton beam reaches 25 GW and the corresponding energy deposition in the SNS mercury target is estimated to be over 6 MJ/m^3/pulse. Such a high-intensity proton beam is essential for the generation of the world's most powerful neutron pulses. Meanwhile, the rapid heating of the mercury from individual proton pulses also induces a large pressure surge in the liquid metal which causes dynamic displacements and stresses to occur in the vessel structure [1]. In particular, the fatigue and cavitation due to pressure waves have a strong impact on the target vessel lifetime [2-4]. To fully understand the dynamic response of the target during operation, it is important to experimentally measure the target strain waveform after each proton pulse injection.

Measurement of dynamic strains in the SNS mercury target is subject to several strict restrictions in the sensor specifications and deployment – limited space, existence of strong electro-magnetic field, high radiation, and fast transient waveforms. While fiber-based strain sensors offer a sound solution in this case, conventional fiber-optic sensors [5-8] either cannot survive radiation levels in the SNS target module or lack sufficient bandwidth to resolve the strain waveform induced by intense proton pulses.

This paper describes the first measurement of the dynamic strains on the spallation target vessel by using high-radiation-tolerant fiber-optic strain sensors developed at SNS. The sensor consists of a low-finesse Fabry-Perot interferometer (FPI) formed by fluorine-doped single-mode fibers. The signal interrogation technique employs a digital phase demodulation scheme reported in our previous work [9]. The radiation-resistance of the fiber has been experimentally verified in this work at an accumulated radiation dose of 10^9 Gy and an acute dose rate of up to 3 kGy/s. Two measurement results are reported in this paper. First, the sensors have displayed sufficiently high bandwidth to resolve the transient strain waveforms induced by the intense proton pulses. The measured strain waveforms have been compared against numerical results. Second, the sensors have survived radiation doses of more than 10^9 Gy. For the first time, we were able to measure the strain profile until the end of the SNS target operation cycle using a fiber-optic sensor. The sensor performance in the high radiation environment is discussed.

II. Sensor Instrumentation and Installation

A. Sensing Interferometer

The present fiber-optic sensor is fabricated using fluorine-doped single-mode fibers from Fujikura (Model RRSMFB) that demonstrated high radiation resistance in the previous work [10,11]. The fiber has a cladding diameter of 125 μm and a core mode-field diameter of 8.7 μm at 1300 nm. Both the core and cladding of the fiber are fluorine-doped SiO_2 with different fluorine concentration ratios. Unlike other radiation-hardening optical fibers that typically have high OH concentration, the OH concentration in the current fiber core is lowered to optimize its transmission performance in the long wavelength region. The standard transmission loss is 0.38 dB/km around 1300 nm and the radiation-induced loss of the fiber has been previously measured to be ~ 2 dB/km in a total dose of 10^4 Gy [11].

This manuscript has been authored by UT-Battelle, LLC under Contract No. DE-AC05-00OR22725 with the U.S. Department of Energy. The United States Government retains and the publisher, by accepting the article for publication, acknowledges that the United States Government retains a non-exclusive, paid-up, irrevocable, world-wide license to publish or reproduce the published form of this manuscript, or allow others to do so, for United States Government purposes. The Department of Energy will provide public access to these results of federally sponsored research in accordance with the DOE Public Access Plan (http://energy.gov/downloads/doe-public-access-plan).

The authors are with Spallation Neutron Source, Oak Ridge National Laboratory, 1 Bethel Valley Road, Oak Ridge, TN 37831, USA. (email: liuy2@ornl.gov)

Many interferometer-based fiber-optic sensors are low-finesse FPIs formed by assembling fibers inside a glass capillary tube. Recently, low-finesse FPI-based fiber-optic sensors were also fabricated by micro-machining fibers or ferrules in a cantilever configuration [12,13]. The sensors were used to measure vibration or acceleration. Fig. 1(a) shows schematic of the current sensor head. It consists of cleaved end surfaces of two pieces of fibers assembled inside a glass tube that has an outer diameter of 209 μm and an inner diameter of 127 μm. The fluorine-doped single-mode fiber is used as the lead-in fiber while the reflecting fiber can be any type of fiber with a cladding diameter of 125 μm. For present sensors, the design gap between the two fiber end surfaces is a few tens of micrometers and the sensor length is typically around 6-8 mm.

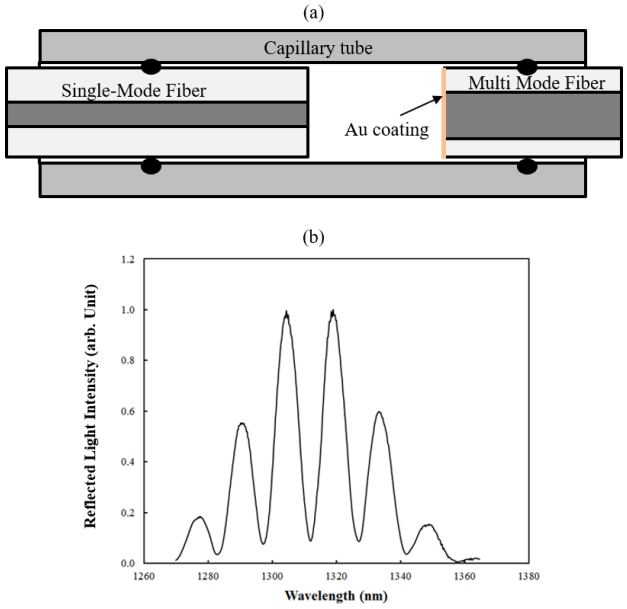

Fig. 1. (a) Schematic of sensor head. (b) Optical spectrum of the reflected light from the sensor. A superluminescent laser diode is used as the light source.

B. Signal Interrogation System

In FPI-based fiber-optic sensors, the measurement of physical quantities is performed through a signal interrogation system that demodulates the interferometric phase containing the optical path difference (OPD) variations in the sensing interferometer. The signal interrogation of the present sensor uses a low-coherence interferometry (LCI) scheme [14] which normally consists of a broadband light source and a local optical processor. The LCI scheme is particularly favorable to our application since it has a high tolerance to the intensity fluctuations of the reflected light and ambient optical noise from the sensor head and the connection fiber cable. A fiber coupled superluminescent laser diode (SLD) is used as the light source. The SLD (Thorlabs S5FC1018S) has a center wavelength of 1320 nm and a spectrum bandwidth of ~ 40 nm at a power level of 15 mW. Fig. 1(b) shows the optical spectrum of the reflected light from the sensing interferometer. The modulation pattern of the spectrum is a result of interference from the FPI. The modulation depth is optimized by adding a customized thin film coating of Au to the polished surface of the reflecting fiber at the Center for Nanophase Materials Sciences (CNMS) at ORNL.

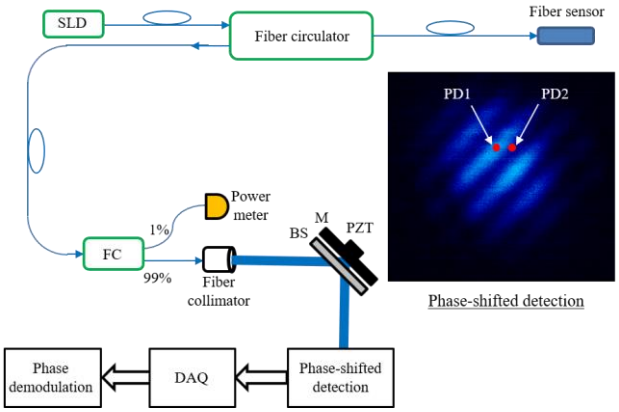

Fig. 2. Schematic of the interrogation optical setup based on a Fizeau interferometer. PD: photo-detector, FC: fiber coupler, M: mirror, BS: 50/50 beam splitter, PZT: piezo-electric transducer actuator. Inset box: two photo-detectors are arranged to generate phase-shifted signals.

A schematic of the entire sensor setup is shown in Fig. 2. The reflected light from the sensor is coupled into a free-space local receiving interferometer (LRI). The LRI is comprised of two pieces of reflectors forming a Fizeau interferometer. The angle between the two reflectors is quite flexible but is typically set around 0.1° ~ 0.3°. The first reflector is a 50/50 beam splitter while the second one is a high reflectivity (HR) mirror that is mounted to a compact translational stage driven by a piezo-transducer (PZT) actuator. The gap between the two reflectors, which is related to the OPD of the LRI, can be precisely controlled by the computer through the PZT driver. When the OPD of the LRI matches that of the FPI in the sensor, an interference pattern is observed at the output of the LRI. Fig. 3 shows the implementation of the LRI. The LRI unit has a dimension of 5″×4″×2″ and four LRI units are integrated in one chasis.

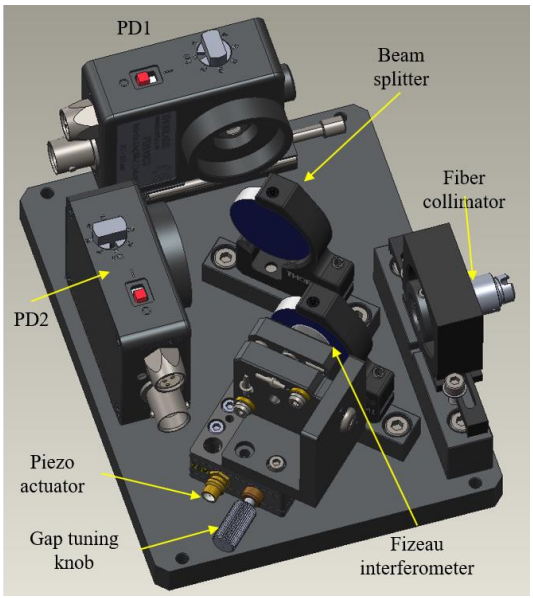

Fig. 3. Implementation of local receiving interferometer for signal interrogation.

We proposed a digital phase demodulation approach based on phase-shifted detection of the interference signal. Two photo-detectors (PDs) are properly positioned on the interference fringes to detect the interference signal with a phase shift. As shown in Fig. 3, the LRI output is split into two PDs using a beam splitter. Positions of two PDs can be adjusted by compact translation stages to generate proper phase shifts. The PD outputs are digitized using a 14-bit National Instrument (NI) data acquisition (DAQ) module (Model PXIe-5170R). The bandwidth of the PDs is tunable up to 10 MHz and the maximum sampling rate of the DAQ is 250 MHz. The phase demodulation calculation is conducted in a computer. The proposed phase demodulation approach enables an in-situ calibration of the phase shift and signal amplitude and therefore shows an excellent adaptability to both the light power fluctuations in the sensor output and the sensor gap variations. In our previous work [9,13], we successfully demodulated phase changes caused by large variations (up to the coherence length of the light source). As discussed in Ref. [9], the DAQ module used in our system can support a maximum measurement amplitude-bandwidth product of 13 μm·MHz. Using the present strain sensor configuration, we are able to obtain a 2 MHz measurement bandwidth when measuring a dynamic strain with an amplitude of 1000 με. This bandwidth is an order of magnitude higher than commercial products such as the Veloce fiber-optic conditioner from FISO Technologies.

C. *Sensor Installation in the Mercury Target Module*

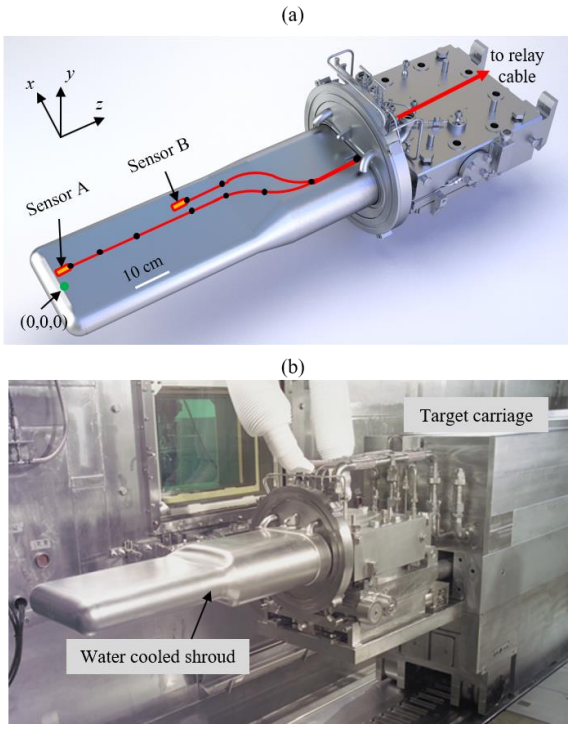

Fig. 4. (a) Sensors mounted on the mercury target vessel. Black dots indicate epoxy spots. Location (0, 0, 0) shows the reference point for coordinates. (b) Target module (mirrored image) mounted on target carriage in the target service bay. The target vessel is covered by water cooled shroud during operation.

The first strain measurement using the developed single-mode fiber-optic sensors and signal interrogation system was conducted in the SNS target T15 (the 15th target used in the SNS operation since 2006). T15 was commissioned in the beginning of October 2016 and was in service until the end of December 2016. The final configuration of the developed fiber sensor consists of a 1-cm-long glass tube and a 2.5-meter-long lead fiber cable made from the same fluorine-doped single-mode fiber. The lead fiber cable has a polyimide coating with a diameter of 250 μm to fit in the interstitial space between the mercury vessel and its water-cooled shroud.

Fig. 4(a) shows the mercury target vessel with the fiber-optic strain sensors mounted on the surface. Sensors and lead fiber cables are glued to the mercury vessel using a Stycast 2850FT epoxy cured with Catalyst 11. The water-cooled shroud is mounted over the mercury vessel after the sensor installation. Lead fiber cables are bundled together and pass through a 5-cm long, 6-mm diameter feedthrough tube which provides a gas barrier seal for the interstitial space. A picture of the assembled target module in the target service bay is shown in Fig. 4(b). Fiber sensors are connected to the signal interrogation system through two relay fiber cables. The first relay fiber cable is designed to run the length (~12 m) of the target carriage. The second relay cable is a 10-meter long feedthrough cable that runs through the penetration between the target service bay (high radiation area) and the target manipulators gallery where the signal processing and other control electronics are located. Connection between the first and second relay cables is conducted using remote handling equipment after the installation of the target module in the service bay. All fiber connectors are angle polished to avoid unwanted reflections to the signal interrogation system.

TABLE I
COORDINATES AND RADIATION DOSE OF SENSORS AND THEIR LEAD FIBER CABLES

Sensor A		Sensor B	
Position (cm)	Radiation Dose (MGy/MWHr)	Position (cm)	Radiation Dose (MGy/MWHr)
6.6, 5.2, 1.0	16.161	12.7, 5.2, 50.5	0.419
6.5, 5.2, 6.0	16.644	12.6, 5.2, 54.8	0.280
7.4, 5.2, 19.6	9.071	11.5, 5.2, 57.4	0.251
7.9, 5.2, 30.0	5.333	3.9, 5.2, 60.0	0.305
7.6, 5.2, 39.3	1.895	0.2, 5.2, 63.0	0.260
6.4, 5.2, 43.7	1.151	0.2, 5.2, 65.5	0.205
4.7, 5.2, 47.6	0.988	2.2, 5.2, 67.4	0.190
1.5, 5.2, 53.1	0.591	14.4, 5.5, 69.4	0.094
-3.5, 5.2, 60.5	0.284	17.8, 6.5, 80.6	0.044
-4.0, 5.2, 62.7	0.234	12.9, 9.1, 92.1	0.027

The location of the sensor and the path of the sensor lead fiber cable on the mercury vessel are recorded for radiation dose calculation. As shown in Fig. 4(a), the path is represented by multiple spots where epoxy is applied. Coordinates of all spots are recorded after the installation. The radiation dose (or the absorbed dose) along the fiber cable is calculated based on the energy deposition from all particles including neutrons, protons, and photons on the target vessel. Therefore, the radiation dose is a function of both the proton beam energy (in the unit of MWHr or 3.6 GJ) and the coordinates (x, y, z) on the mercury vessel surface. Table I lists the coordinates and the estimated radiation dose of the first 10 spots of the two single-mode sensors. The peak radiation doses (usually occur at the

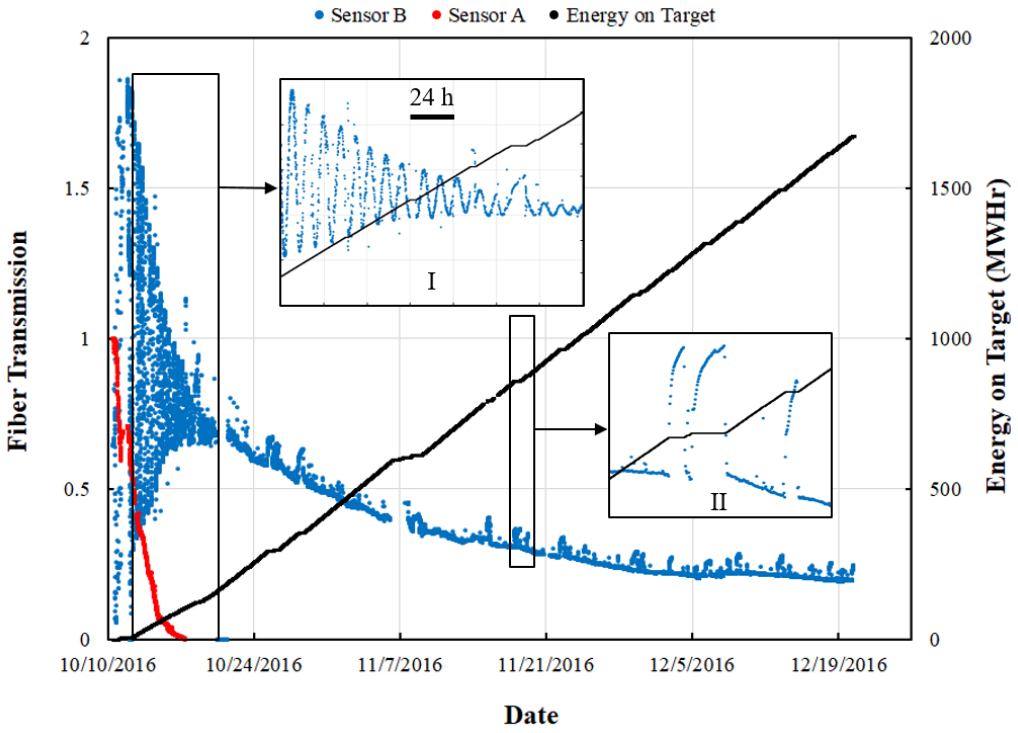

Fig. 5. Normalized fiber transmission from the fiber sensors and proton beam energy delivered on the mercury target during the SNS operation period from Oct. 10, 2016 to Dec. 20, 2016. Inset box I: periodic oscillations of the measured RIA over 10 days of sensor B measurement. Inset box II: fiber transparency 'recovery' during the proton beam off period. The power measurement was stopped in a few cases.

sensor head) are used to evaluate the maximum radiation tolerance of the sensor. For sensors A and B shown in Fig. 4(a), the peak radiation doses are 16.64 and 0.42 MGy/MWHr, respectively. Unlike other RIA measurements where a uniform radiation dose was applied to the test fiber cable, the fiber cable in the current experiment receives a location-dependent radiation. In particular, the radiation dose shows an exponential decay along the proton beam propagation direction. To precisely evaluate the radiation-induced effect on the fiber, we integrated the radiation dose along the fiber cable path. Since the radiation level beyond the target vessel is much lower, the integration is conducted on the fiber inside the interstitial space only. The calculated integrals are 2.61 MGy·m/MWHr and 66 KGy·m/MWHr for the fiber cables of sensors A and B, respectively.

III. MEASUREMENT RESULTS

A. Radiation-Induced-Attenuation (RIA) Measurement

As shown in Fig. 2, a small portion (~ 1%) of the reflected light from the sensor is directly coupled into a slow detector to monitor its power variation. The fiber transmission, which is defined as the ratio of the reflected light power from the sensor to the incident light power, is used to calculate the RIA of the optical fiber. In previous RIA measurements [10,16,17] of the fluorine-doped fiber, the maximum dose rate was around 1 Gy/s and the total radiation dose was limited 10^6 Gy level, although higher radiation doses were used in the RIA measurement of different types of fibers [18]. On the other hand, in the interstitial space of the SNS mercury target, the estimated radiation dose rate can exceed 10^3 Gy/s and the peak radiation dose can reach 10^9 Gy, both of which are three orders of magnitude higher than the irradiation conditions in the previous RIA measurements of fluorine-doped fibers.

Fig. 5 shows the measured fiber transmission (normalized to the initial value taken right after the first proton pulse was delivered on the target) from the two sensors over the entire target operation period. The radiation dose at each marked location in Table I is calculated based on the proton beam energy. The proton beam energy delivered on the target is also plotted to show the status of radiation. Flat line segments in the beam energy plot correspond to beam-off states, i.e. when the proton beam is off from the target.

The two sensors show quite different fiber transmission variations. For sensor A, the fiber transmission shows a monotonic reduction as a function of the proton beam energy. For sensor B, however, the fiber transmission shows damped oscillations in the first two weeks. As revealed more clearly in the inset box I, the period of the oscillations is about 9 hours and the oscillations stop when the proton beam is off from the target, which strongly suggests that the oscillations are directly related to the proton beam. The mechanism for the damped oscillations is considered as follows. When the target receives neutron-production proton beam, the high radiation around the sensor head induces a slight expansion of the epoxy which causes a continuous increase of the sensor gap, i.e., the gap of the FPI inside the capillary tube. Since sensor B has a short default gap (~ 40 μm) that is not much longer than the coherence length (~ 30 μm) of the light source, interference

exists between the direct light reflections from the FPI. In other words, the observed damped oscillations are the interference signal from the FPI modified by the coherence function of the broadband light source [14]. From Fig. 5, we can calculate that the gap of the sensor extended by 12 μm over the first two weeks, which corresponds to about 0.2% expansion ratio of the capillary tube. Clearly, as the sensor gap becomes significantly longer than the coherence length of the light source, direct interference from the sensor can no longer be observed and the fiber transmission of sensor B is only dominated by the RIA of the fiber. The gap of sensor A is around 60 μm which is twice of the coherence length of the light source and therefor no direct interference has been observed in its fiber transmission curve. It should be emphasized that the intensity variation of the reflected light does not affect the strain measurement results, as will be shown in the next sections.

Another interesting observation is the recovery behavior of the fiber transmission. An example is shown in the inset box II. When the proton beam is turned off, the fiber transmission shows a quick increase, or a recovery. Such a gain of the fiber transmission is only temporary. Once the proton beam is resumed, the gained transparency of the fiber is quickly lost regardless of the amount of the gain acquired during the beam-off time. The temporary recovery of the fiber transparency is due to thermal annealing of the defects which are quickly re-activated upon the resume of radiation [17, 18].

Finally, the RIA for fibers of both sensors have been calculated in the following. For sensor A, we measured the fiber transmission attenuation to be 10.9 dB at an accumulated proton beam energy of 77 MWHr. The corresponding integral of the radiation dose along the fiber cable is 201 MGy·m. The RIA of the fiber for sensor A is therefore calculated to be 5.4×10^{-8} dB/Gy/m. For sensor B, we estimated the fiber RIA based on the measured attenuation data during Oct. 22 and Dec. 20 to eliminate the influence from the sensor gap extension. During this time period, the attenuation is 5.4 dB and the accumulated proton beam energy is 1470 MWHr. The integral of the radiation dose along the fiber cable is 97.0 MGy·m and the corresponding RIA of the fiber is calculated to be 5.6×10^{-8} dB/Gy/m. Both numbers are much lower than the RIA value (~ 2×10^{-7} dB/Gy/m) previously measured in low radiation doses [11]. Note that the RIA estimations from the two sensors are very close to each other, even though there is a substantial difference in the radiation dose rates between the two sensors.

B. Strain Measurement of On-Demand Test Proton Pulses

At the beginning of the target commissioning, a series of on-demand test pulses of the proton beam were sent to the mercury target to calibrate the sensor operation and investigate strain waveforms at different power levels of the proton beam. The test pulses were varied in protons per pulse to represent equivalent power levels at 60 Hz from the beam power of 0.1 to 1.4 MW. Fig. 6 shows an example of the strain measurement result (from sensor A) including (a) the measured phase-shifted PD output waveforms and (b) the recovered strain waveform from the PD output. The inset box in Fig. 6(a) shows the fast variation waveform of the detector output. Each measurement normally requires 50-ms long time series that covers three strain

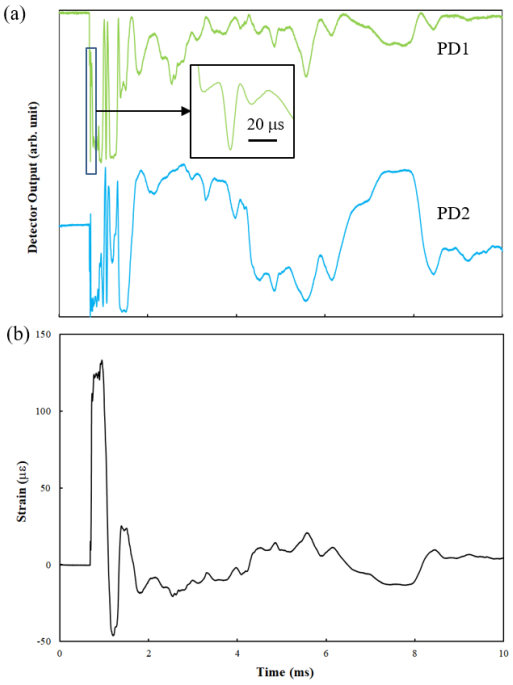

Fig. 6. A typical strain measurement result of the 1.4 MW proton pulse. (a) Phase-shifted output waveforms (normalized) from two PDs. Inset box: detailed structure of the PD output during rising edge of the strain pulse. (b) Recovered strain waveform.

pulses. At the end of the measurement, a 40-ms long, ~2-μm amplitude modulation signal is automatically applied to the piezo actuator of the LRI for calibration of the PD output amplitude. The real-time calibration procedure significantly improves the measurement accuracy and eliminates the influence of the power fluctuations in the sensor output [9].

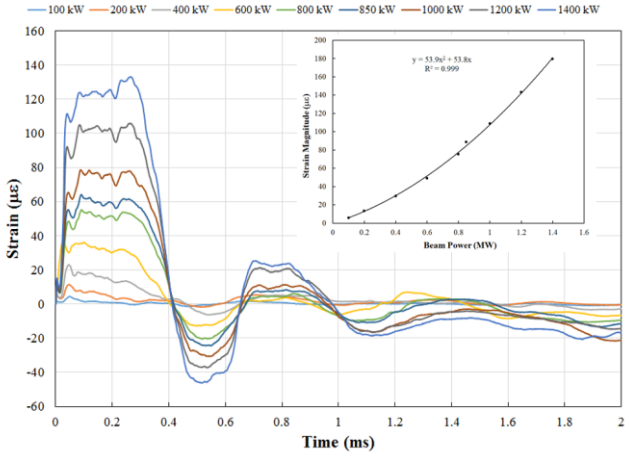

Fig. 7. Strain waveforms measured with sensor A at different (equivalent) power levels of the proton beam. Inset box: strain magnitude vs. proton beam power.

Fig. 7 shows the measured strain waveforms from sensor A at different (equivalent) proton power levels. A typical strain waveform consists of a main pulse and relaxation oscillations. The main strain pulse is considered to be the response of the stainless-steel shell to the pressure wave directly induced by the proton pulse. The rising edge of the strain pulse gets sharper as the proton beam power increases. The estimated rising time of

the strain waveform of the 1.4 MW proton pulse is about 10 μs. Therefore, a measurement bandwidth of over 100 kHz is necessary to resolve the temporal structure of the strain waveform. For the current strain measurement, the PD bandwidth is set at 300 kHz and the sampling rate of the DAQ is 10 MHz. While the proton pulse width is only 700 ns, the measured strain pulse width is about 300 μs due to slower response of the target vessel material. The relaxation oscillations last over a few milli-seconds with a period of about 600 μs. Such oscillations are caused by the fluid-structure interactions excited by the impulsive load of the proton beam pulse [2]. The measured strain magnitude (peak-to-peak value in Fig. 7) is plotted as a function of the (equivalent) proton beam power in the inset box of Fig. 7. We found that the strain magnitudes can be well fit with a quadratic function of the proton beam power in this case.

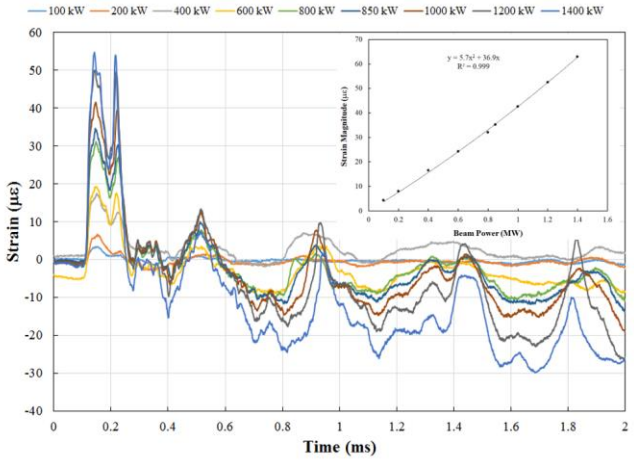

Fig. 8. Strain waveforms measured with sensor B at different (equivalent) power levels of the proton beam. Inset box: strain magnitude vs. proton beam power.

Fig. 8 shows the measured strain waveforms from sensor B at various (equivalent) proton power levels. The results are very different from those measured from sensor A. There is a ~90 μs time delay between the first strain pulses, which accounts for the propagation time of the pressure wave between the locations of two sensors. The primary strain pulse measured from sensor B shows a much narrower pulse width (100 μs versus 300 μs of sensor A) with a break-up in the middle of the pulse. The strain magnitude is much lower compared to sensor A. The strain magnitude versus the proton beam power is plotted in the inset box of Fig. 8. Unlike sensor A, the power dependence of the strain magnitude in the case of sensor B is dominated by a linear function. The different responses at sensors A and B are a manifestation of the complex response of the target fluid-structure system to the 700-ns proton beam pulse load. Local strain responses are influenced by the proton pulse energy deposition, the propagation of pressure through the target, sound speed changes due to mercury cavitation, and local vessel stiffness and inertia variations. Sensor A – being forward in the target – sees response to the pressure from the proton beam energy more directly, whereas sensor B is mostly out of a region of direct proton beam energy deposition and is responding more to the pressure wave propagation.

C. *Strain Measurement of Neutron Production Pulses*

The SNS target was switched to the neutron production mode after the initial test. The proton beam power was ramped to 850 kW in the first week and was then increased to 1.2 MW in the second week. The same proton power was maintained until the end of the operation cycle. The strong radiation tolerance of the fiber and the signal interrogation technique used in the present sensors enabled strain measurements over a long time during the neutron production period.

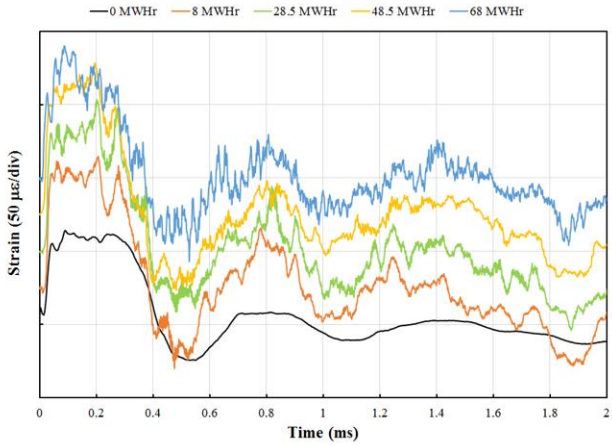

Fig. 9. Strain waveforms of test pulse and neutron production beam measured from sensor A. Index shows the proton beam energy delivered on the target when the measurement was taken. 0 MWHr corresponds to the test pulse case. Plots are vertically shifted. Proton beam power is 850 KW. Other parameters are listed in Table II.

TABLE II
PARAMETERS FOR FIG. 9 (PROTON BEAM POWER: 850 KW)

Measurement Date	Energy on Target (MWHr)	Cumulative Radiation Dose (Gy)	Fiber Transmission	Strain Magnitude (με)
10/10/2016	0	~ 10^5	1	88.6
10/12/2016	8	1.3×10^8	0.55	144.7±6.1
10/13/2016	28.5	4.6×10^8	0.34	160.8±4.1
10/14/2016	48.5	7.9×10^8	0.18	156.6±5.4
10/15/2016	67.9	1.1×10^9	0.06	147.7±5.4

Fig. 9 shows the measured strain waveforms from sensor A after the neutron production started. The proton beam power was set at 850kW. The strain waveform of the test pulse is also shown as a reference. This sensor is located right next to the proton beam interaction point where the estimated dose rate is 3.8 kGy/s. Parameters for each measurement are listed in Table II. The overall strain waveform structure and the width of the first strain pulse are similar to that measured on the test pulse. Two remarkable differences between the strain waveforms of the neutron production beam and that of the test pulse are noted. First, the strain magnitude (140 – 160 με) of the neutron production beam is about 60% higher than that of the test pulse. Next, the strain waveform of the neutron production beam shows high-frequency oscillations and the high-frequency components grow as the radiation dose increases. We consider both of them might be caused by the radiation-induced epoxy hardening during neutron production, which results in stronger bond of the sensor to the stainless-steel vessel and increases the stiffness of the sensor head to the mechanical vibrations. The

high-frequency oscillations could also be associated with cavitation.

As shown in Fig. 5, sensor B has substantial fiber transmission until the end of the target operation cycle and the sensor provided valid strain measurements through the entire operation cycle. Fig. 10 shows the strain waveforms measured from sensor B at different times. The target was operating at 1.2 MW in all cases. Parameters of the measurements are summarized in Table III. Note that the last strain measurement was taken only minutes before the end of the target operation cycle. The sensor survived through the entire cycle of the target with an accumulated dose of 7×10^8 Gy. Compared with sensor A, the strain magnitude during neutron production beam increased only about 15% over that of the test proton pulse and high-frequency oscillations are weak and only start to appear in the last two strain waveforms. We consider this is because the radiation dose rate is much lower in the location of sensor B. As shown in Table III, the strain magnitude of the neutron production beam stays quite stable within 85 to 90 με over the entire operation time period. The main strain pulse shows a gradual broadening from the initial 100 μs to about 200 μs at the end. We speculate that such a pulse broadening was possibly caused by the change of the dynamic response of the target vessel over the time due to fatigue and cavitation damage [19,20].

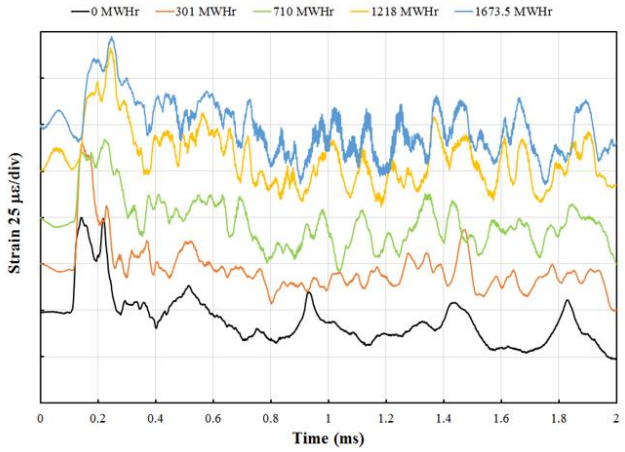

Fig. 10. Strain waveforms of test pulse and neutron production beam measured from sensor B. Index shows the proton beam energy delivered on the target when the measurement was taken. 0 MWHr corresponds to the test pulse case. Plots are vertically shifted. Proton beam power is 1200 KW. Other parameters are listed in Table III.

TABLE III
PARAMETERS FOR FIG. 10 (PROTON BEAM POWER: 1200 KW)

Measurement Date	Energy on Target (MWHr)	Cumulative Radiation Dose (Gy)	Fiber Transmission	Strain Magnitude (με)
10/10/2016	0	~ 10^5	1	76.4
10/26/2016	301	1.3×10^8	0.91	90.8±4.7
11/12/2016	710	3.0×10^8	0.87	85.7±3.0
12/02/2016	1218	5.1×10^8	0.50	88.0±3.7
12/20/2016	1674	7.0×10^8	0.34	84.6±3.7

The temperature of the target vessel is also monitored using thermal sensors [21]. Gradual temperature changes are observed when the proton beam power is varied. Since the temperature change is slow, it only affects the baseline of the strain waveform.

A sensor is considered to reach its lifetime when it can no longer provide consistent strain measurements. Sensor A survived a proton beam energy of 77 MWHr and the accumulated radiation dose at the sensor head is calculated to be 1.3×10^9 Gy. Meanwhile, sensor B survived to the end of the target operation cycle with a total proton beam energy of 1674 MWHr. The accumulative radiation dose at the sensor head is 7×10^8 Gy. Using the similar criterion, we have also evaluated the lifetime of commercial fiber-optic sensors from FISO installed on the same target vessel. The commercial sensors located near sensor A survived radiation doses of up to 10^8 Gy while those near sensor B survived radiation doses of up to 5×10^7 Gy [21]. The results show that the developed single-mode fiber sensors have an order of magnitude longer lifetime (in terms of the radiation dose) than their commercial counterparts.

D. *Comparison between Measurements and Simulations*

The measurement results have been compared with the preliminary numerical simulations from the target analysis. The analysis was performed using an empirical model for mercury developed to represent cavitation [1]. Fig. 11 shows two pairs of strain waveforms obtained from measurement (solid lines) and simulation (dashed lines) at a proton beam power of 1.4 MW. Clearly the measurements and calculations show similar strain profiles and identical phase delay between two sensors. On the other hand, the measured strain magnitude is about 40% smaller than the calculated result. Further study is required to understand the difference between experimental measurements and numerical predictions.

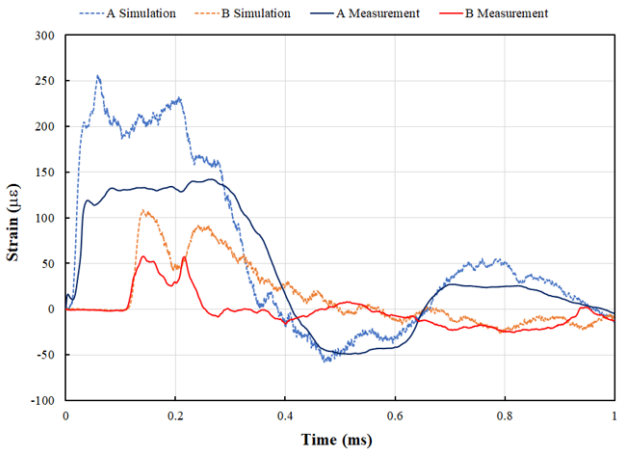

Fig. 11. Comparison between experimental measurement and simulation results. Proton beam power is set at 1.4 MW.

IV. CONCLUSION

We have developed high-radiation-tolerant fiber-optic strain sensors and applied them to the measurement of dynamic strains on the mercury target vessel in the SNS. The sensors are fabricated using fluorine-doped single-mode optical fibers that have high radiation tolerance around 1300 nm. A novel digital phase demodulation scheme has been employed in the signal

interrogation system, which enables effective strain measurement independent of light intensity fluctuations and sensor gap variations. Transient strain waveforms induced by high energy, high intensity proton pulses have been successfully measured by two sensors. The RIA of the fiber and the sensor lifetime have been experimentally investigated. The sensors have survived radiation doses of over 10^9 Gy. Using the developed sensors, we were able to monitor the strain waveform of the neutron production beam at some locations of the target vessel until the end of the target operation cycle. Strain waveforms of neutron production beam are consistent in the strain profile and magnitude. Compared to the test proton pulse measurement, the strain waveform of the neutron production beam shows a number of new features including strain magnitude increase, pulse width broadening, and high-frequency components in the waveform. The measurement results have been compared with numerical simulations. Since this is the first-time strain measurement of the neutron production beam in the SNS target, the mechanisms for some observations are not well understood and need further study.

The strain measurement using the developed fiber-optic sensors provides a useful tool for the study of dynamic response of the spallation mercury target materials and other applications involving high radiation environment and high measurement bandwidth requirement. In particular, the high-radiation-tolerant sensors will be used to evaluate the efficacy of the gas injection method which has been investigated as an important strain mitigation approach in recent years [4].

ACKNOWLEDGMENT

We acknowledge R. Sangrey, J. Bryan, S. Murray, III, D. Hensley, A. Menshov, and W. Lu for their technical help.

REFERENCES

[1] J. R. Haines, T. J. McManamy, T. A. Gabriel, R. E. Battle, K. K. Chipley, J. A. Crabtree, L. L. Jacobs, D. C. Lousteau, M. J. Rennich, and B. W. Riemer, "Spallation neutron source target station design, development, and commissioning," Nucl. Instrum. Methods Phys. Res. A 764, 94-115 (2014).

[2] B. W. Riemer, "Benchmarking dynamic strain predictions of pulsed mercury spallation target vessels," J. Nucl. Mater. 343, 81-91 (2005).

[3] M. Futakawa, H. Kogawa, S. Hasegawa, Y. Ikeda, B. Riemer, M. Wendel, J. Haines, G. Bauer, T. Naoe, K. Okita, A. Fujiwara, Y. Matsumoto, and N. Tanaka, "Cavitation damage prediction for spallation target vessels by assessment of acoustic vibration," J. Nuclear Mater. 377, 182-188 (2008).

[4] B. W. Riemer, M. W. Wendel, D. K. Felde, R. L. Sangrey, A. Abdou, D. L. West, T. J. Shea, S. Hasegawa, H. Kogawa, T. Naoe, C. H. Farny, A. L. Kaminsky, "Small gas bubble experiment for mitigation of cavitation damage and pressure waves in short-pulse mercury spallation targets," J. Nucl. Mater. 450, 192-203 (2014).

[5] G. Cheymol, A. Gusarov, S. Gaillot, C. Destouches, and N. Caron, "Dimensional measurements under high radiation with optical fibre sensors based on white light interferometry - report on irradiation tests," IEEE Trans. Nucl. Sci., vol. 61, no. 4, pp. 2075–2081, Aug. 2014.

[6] Y. Sun, D. Liu, P. Lu, Q. Sun, W. Yang, S. Wang, L. Liu, and J. Zhang, "Dual-parameters optical fiber sensor with enhanced resolution using twisted MMF based on SMS structure," IEEE Sensors Journal, Vol. 17, NO. 10, 3045-3051 (2017).

[7] Y. Ouyang, H. Guo, X. Ouyang, Y. Zhao, Z. Zheng, C. Zhou, and A. Zhou, "An in-fiber dual air-cavity Fabry-Perot interferometer for simultaneous measurement of strain and directional bend," IEEE Sensors Journal 17, 3362-3366 (2017).

[8] A. K. Sang, M. E. Froggatt, D. K. Gifford, S. T. Kreger, and B. D. Dickerson, "One centimeter spatial resolution temperature measurements in a nuclear reactor using Rayleigh scatter in optical fiber," IEEE Sensors Journal 8, 1375-1380 (2018).

[9] Y. Liu, R. Strum, D. Stiles, C. Long, A. Rakhman, W. Blokland, D. Winder, B. Riemer, M. Wendel, "Digital phase demodulation for low-coherence interferometry-based fiber-optic sensors," Opt. Commun. 411, 27-32 (2018).

[10] K. Sanada, N. Shamoto, and K. Inada, "Radiation resistance of fluorine-doped silica-core fibers," J. Non-Cryst. Solids 179, 339-344 (1994).

[11] K. Aikawa, K. Izoe, N. Shamoto, M. Kudoh, and T. Tsumanuma, "Raidation-resistant single-mode optical fibers," Fujikura Technical Review 9-13 (2008).

[12] A. Cipulloa, G. Gruca, K. Heeck, F. De Filippis, D. Iannuzzi, A. Minardoa, L. Zeni, "Numerical study of a ferrule-top cantilever optical fiber sensor for wind-tunnel applications and comparison with experimental results," Sensors and Actuators A 178, 17-25 (2012).

[13] J. Li, G.Y. Wang, J. N. Sun, R. R. J. Maier, W. N. Macpherson, D. P. Hand, and F. Z. Dong, "Micro-machined optical fiber side-cantilevers for acceleration measurement," IEEE Photon. Technol. Lett. 29, 1836-1839 (2017).

[14] Y. J. Rao and D. A. Jackson, "Recent progress in fibre optic low-coherence interferometry," Meas. Sci. Technol. 7, 981-999 (1996).

[15] Y. Liu, W. Blokland, J. Bryan, A. Rakhman, B. Riemer, R. Sangrey, R. Strum, M. Wendel, D. Winder, "Radiation-resistant fiber optic strain sensors for SNS target instrumentation," Proc. of IPAC, Busan, Korea, pp. 371-373 (2016).

[16] T. Wijnands, L. K. de Jonge, J. Kuhnhenn, S. K. Hoeffgen, and U. Weinand, "Optical absorption in commercial single mode optical fibers in a high energy physics radiation field," IEEE Trans. Nucl. Sci. 55, 1-7 (2008).

[17] G. Cheymol, H. Long, J. F. Villard, and B. Brichard, "High level Gamma and neutron irradiation of silica optical fibers in CEA OSIRIS nuclear reactor," IEEE Trans. Nucl. Sci., vol. 55, no.4, pp. 2252–2258, Aug. 2008.

[18] S. Girard, J. Kuhnhenn, A. Gusarov, B. Brichard, M. van Uffelen, Y. Ouerdane, A. Boukenter, and C. Marcandella, "Radiation effects on silica-based optical fibers: recent advances and future challenges," IEEE Trans. Nucl. Sci. 60 (3), 2015-2036 (2013).

[19] B. W. Riemer, J. Janney, S. Kaminskas, D. McClintock, and P. Rosenblad, "Target operational experience at the Spallation Neutron Source," Proc. 11th Int'l Toptical Meeting on Nuclear Applications of Accelerators (AccApp 2013), Bruges, Belgium, pp. 359-365 (2013).

[20] D. McClintock, B.W. Riemer, P.D. Ferguson, A.J. Carroll, M.J. Dayton, "Initial observations of cavitation-induced erosion of liquid metal spallation target vessels at the Spallation Neutron Source," J. Nucl. Mater. 431, 147-159 (2012).

[21] W. Blokland, Y. Liu, B.W. Riemer, M.W. Wendel, and D.E. Winder, "Strain and temperature measurements from the SNS mercury target vessel during high intensity beam pulses", Proc. 8th Int. Particle Accelerator Conf. (IPAC'17), Copenhagen, Denmark, pp. 1230-1233 (2017).